

Modes of massive nucleon transfer appearing in quasifission processes for collisions of superheavy nuclei

Shota Amano ¹, Yoshihiro Aritomo ¹, and Masahisa Ohta ²¹*Kindai University, Higashi-Osaka, Osaka 577-8502, Japan*²*Konan University, Kobe, Hyogo 658-8501, Japan* (Received 8 March 2022; revised 21 June 2022; accepted 26 July 2022; published 17 August 2022)

Background: It is challenging to distinguish between fusion-fission and quasifission experimentally. To determine the characteristics of quasifission processes associated with dominant phenomena in heavy-ion collisions is important for estimating precisely the fusion cross section, which is relevant to the synthesis of new elements. We classified fusion-fission and quasifission processes theoretically in the past for an accurate assessment of the fusion cross section [Y. Aritomo and M. Ohta, *Nucl. Phys. A* **744**, 3 (2004)]. However, no detailed analysis focused on each process was performed.

Purpose: In this work, we aimed to analyze the dynamical characteristics of quasifission processes in terms of the Langevin equation model. We specify the quasifission processes, and analyze the scission configuration. Finally, we clarify the origin of several modes included in quasifission.

Method: The calculation framework is the multidimensional dynamical model of nucleus-nucleus collisions based on the Langevin equations.

Results: It is shown that several quasifission modes exist leading to different fragment deformations. The timescale of the quasifission process differs for several different modes. Each scission configuration and total kinetic energy also differ.

Conclusions: The different quasifission modes are caused by the neck relaxation controlling the mass drift toward symmetry. This means that it is possible to discuss the time-dependent functional form of the neck parameter ϵ for the quasifission process in the framework of the dynamical model based on Langevin equations.

DOI: [10.1103/PhysRevC.106.024610](https://doi.org/10.1103/PhysRevC.106.024610)

I. INTRODUCTION

Heavy nuclear collisions associated with the large mass transfer between reaction partners have been attracting considerable attention in the last several decades as incomplete fusions and quasifission (QF) processes [1–6]. Various phenomena can be seen in these reactions, depending on the induced angular momentum, i.e., complete fusion producing a compound nucleus (CN), QF, deep inelastic collision (DIC), and quasielastic collision (QEC). The theoretical identification of these phenomena has been traditionally carried out on the basis of the geometrical difference in the impact parameter (or corresponding the angular momentum) of the incident channel. At low impact parameters, complete fusions are dominant. Many QF events are included in the reactions at low-medium impact parameters. For medium-high impact parameters, the dominant reaction type is DIC. When impact parameters is high, QEC is observed. In the quantum-based dinuclear system model [7], QF is described on the basis of the property of the diffusion of nucleons in the mass asymmetry of reaction partners. Multinucleon transfer in the DIC process has been studied by the Langevin-type approach [8]. Here, we apply the Langevin-type approach to investigate the dynamical characteristics of the QF process.

QF processes are considered to be a bridge between DIC, where much relative kinetic energy is transferred to their thermal energy, and CN formation leading to evaporation residue (ER) products after possible particle emissions [3]. The estimation of the ER cross section in the superheavy mass region has been paid much attention in the challenge of new element synthesis. In this sense, the study of the QF mechanisms, that is, the dynamical characteristics of QF and the separation of QF and CNF (CN fission), is important for the precise estimation of the ER cross section. In particular, the study of the dynamics of QF process can be expected to open a new field for the reaction mechanism in the superheavy mass region because the process is related to the mass transfer and the shell structure.

To date, the characteristics of QF have been discussed in the paper on the total kinetic energy (TKE) of fission fragments including the long-standing problem of energy transfer to the kinetic energy of fragments and in the investigation of the timescale of the mass drift to the mass symmetric direction [1].

In this paper, the dynamical characteristics of the QF process are presented by the analysis of dynamical Langevin trajectories using the unified Langevin equation model [9]. This Langevin-type approach was developed by Zagrebaev *et al.* [9] for the analysis of heavy-ion collision from the

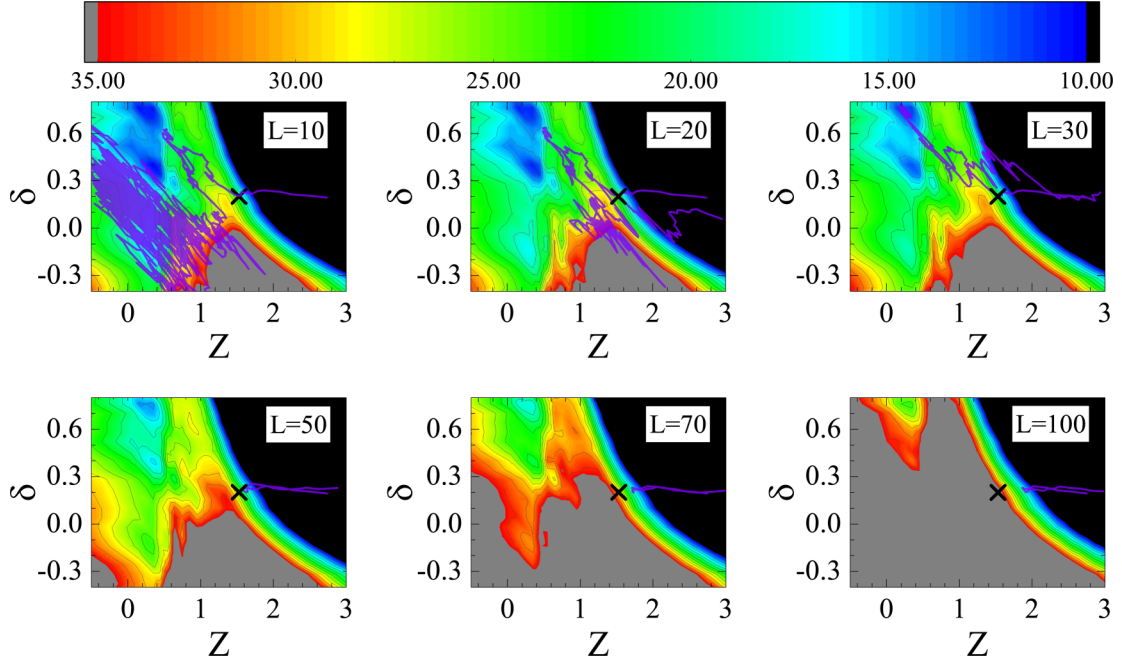


FIG. 1. The sample trajectories and the z - δ plane potential energy surface ($\alpha = 0.78$) for each orbital angular momentum (L) in the $^{26}\text{Mg} + ^{230}\text{Th}$ reaction. The calculation starting point is $\{z, \delta\} = \{2.85, 0.20\}$. The \times marks denote the contact points.

entrance stage to the fused system including fission processes. We have revealed the existence of QF modes in the reactions of the ^{48}Ca projectile and the actinide target system. These QF modes are investigated in connection with their timescale, the distribution of the fragment deformation, and the time evolution of neck formation. In terms of the trajectory analysis of the QF process, we show the reason for the appearance of the mode.

In the following section, a brief introduction of the Langevin-type approach is presented. The dynamical QF characteristics of the $^{48}\text{Ca} + ^{249}\text{Bk}$ system at $E_{c.m.} = 213.05$ MeV are described in Sec. III, where the detailed analyses of the properties of the QF mode and the reason for their appearance are presented. Our concluding remarks are given in the final section.

II. FRAMEWORK

A. Potential energy surface

We adopt a dynamical model that is similar to the unified model [10]. First, the initial stage of the nucleon transfer reactions consists of two parts: (1) the system is calculated in the ground state of the projectile and target because the reaction is too fast for the nucleons to reconfigure a single-particle state. (2) Then, the former system relaxes to the ground state of the entire composite system, which changes the potential energy surface to an adiabatic one. Therefore, we consider the time evolution of the potential energy from the diabatic one $V_{\text{diab}}(q)$ to the adiabatic one $V_{\text{adiab}}(q)$. Here, q denotes a set of collective coordinates representing a nuclear shape. The diabatic potential is calculated by a folding procedure using effective nucleon-nucleon interaction [9–11]. However, the adiabatic potential energy of the system is calculated using an extended

two-center shell model [9]. Then, we connect the diabatic and adiabatic potential energies with a time-dependent weighting function $f(t)$ as follows:

$$V(q, t) = V_{\text{diab}}(q)f(t) + V_{\text{adiab}}(q)[1 - f(t)], \quad (1)$$

$$f(t) = \exp\left(-\frac{t}{\tau}\right). \quad (2)$$

Here, t is the interaction time and τ is the relaxation time in the transition from the diabatic potential energy to the adiabatic one. We use the relaxation time $\tau = 10^{-22}$ s proposed in Refs. [12–14].

We use the two-center parametrizations as coordinates to represent nuclear deformation [15,16]. To solve the dynamical equation numerically and avoid the huge computation time, we strictly limited the number of degrees of freedom and employed three parameters as follows: z_0 (distance between the centers of two potentials), δ (deformation of fragment), and α (mass asymmetry of colliding nuclei); $\alpha = \frac{A_1 - A_2}{A_1 + A_2}$, where A_1 and A_2 not only stand for the mass numbers of the target and projectile, respectively [11,17], but also are then used to indicate the mass numbers of the two fission fragments. A_{CN} is the mass number of the compound nucleus. As shown in Fig. 1 of Ref. [15], the parameter δ is defined as $\delta = \frac{3(a-b)}{2a+b}$, where a and b represent the half length of the ellipse axes in the z_0 and orthogonal-to- z_0 directions, respectively. We assume that each fragment has the same deformation in the first step. In addition, we use scaling to minimize the computation time and use the coordinate z defined as $z = \frac{z_0}{R_{\text{CN}}B}$, where R_{CN} denotes the radius of the spherical compound nucleus and the parameter B is defined as $B = \frac{3+\delta}{3-2\delta}$.

The adiabatic potential energy is defined as

$$V_{\text{adiab}}(q, L, T) = V_{\text{LDM}}(q) + V_{\text{SH}}(q, T) + V_{\text{rot}}(q, L), \quad (3)$$

where V_{LDM} and V_{SH} are the potential energy of the finite-range liquid drop model and the microscopic energy that takes into account the temperature dependence, respectively. The simplified symbol V_{LDM} and the symbol V_{SH} are described as

$$V_{\text{LDM}}(q) = E_S(q) + E_C(q), \quad (4)$$

$$V_{\text{SH}}(q, T) = E_{\text{shell}}^0(q)\Phi(T), \quad (5)$$

$$E_{\text{shell}}^0(q) = \Delta E_{\text{shell}}(q) + \Delta E_{\text{pair}}(q). \quad (6)$$

The symbols E_S and E_C stand for generalized surface energy [18] and Coulomb energy, respectively. The symbol E_{shell}^0 indicates the microscopic energy at $T = 0$, which is calculated as the sum of the shell correction energy ΔE_{shell} and the pairing correlation correction energy ΔE_{pair} . T is the temperature of the compound nucleus calculated from the intrinsic energy of the composite system. ΔE_{shell} is calculated by the Strutinsky method [19,20] from the single-particle levels of the two-center shell model potential [15,21,22] as the difference between the sum of single-particle energies of occupied states and the averaged quantity. ΔE_{pair} is evaluated in the BCS approximation as described in Refs. [20,23]. The averaged part of the pairing correlation energy is calculated assuming that the density of single-particle states is constant over the pairing window. The pairing strength constant is related to the average gap parameter $\bar{\Delta}$ by solving the gap equation in the same approximation and adopting $\bar{\Delta} = 12/\sqrt{A}$ suggested in [23] by considering the empirical results for the odd-even mass difference [24]. The temperature dependence factor $\Phi(T) = \exp(-\frac{E^*}{E_d})$ is explained in Ref. [17], where E^* indicates the excitation energy of the compound nucleus. E^* is given as $E^* = aT^2$, where a is the level density parameter. The shell damping energy E_d is selected as 20 MeV. This value is given by Ignatyuk *et al.* [25]. V_{rot} is the centrifugal energy generated from the total angular momentum L . We obtain

$$V_{\text{rot}}(q, L) = \frac{\hbar^2 \ell(\ell + 1)}{2\mathcal{I}(q)} + \frac{\hbar^2 L_1(L_1 + 1)}{2\mathfrak{S}_1(q)} + \frac{\hbar^2 L_2(L_2 + 1)}{2\mathfrak{S}_2(q)}. \quad (7)$$

Here, $\mathcal{I}(q)$ and ℓ represent the moment of inertia of the rigid body with deformation q and the relative orientation of nuclei and relative angular momentum respectively. The moment of inertia and the angular momentum for the heavy and light fragments are $\mathfrak{S}_{1,2}$ and $L_{1,2}$, respectively.

The neck parameter ϵ entering in the two-center parametrization was adjusted to reproduce the available data, assuming different values between the entrance and exit channels of the reactions [26]. In our study, we use $\epsilon = 1$ for the entrance channel and $\epsilon = 0.35$ for the exit channel. We assume the following time dependence of Eq. (4), expressed in terms of the characteristic relaxation time of the neck t_0 and the variance Δ_ϵ :

$$\begin{aligned} V_{\text{LDM}}(q, t) &= V_{\text{LDM}}(q, \epsilon = 1)f_\epsilon(t) \\ &\quad + V_{\text{LDM}}(q, \epsilon = 0.35)[1 - f_\epsilon(t)], \\ f_\epsilon(t) &= \frac{1}{1 + \exp\left(\frac{t-t_0}{\Delta_\epsilon}\right)}. \end{aligned} \quad (8)$$

B. Dynamical equations

We perform trajectory calculations of the time-dependent unified potential energy [10,11,17] using the multidimensional Langevin equation [11,17,27] as follows:

$$\begin{aligned} \frac{dq_i}{dt} &= (m^{-1})_{ij}p_j, \\ \frac{dp_i}{dt} &= -\frac{\partial V}{\partial q_i} - \frac{1}{2}\frac{\partial}{\partial q_i}(m^{-1})_{jk}p_jp_k - \gamma_{ij}(m^{-1})_{jk}p_k \\ &\quad + g_{ij}R_j(t), \\ \frac{d\vartheta}{dt} &= \frac{\ell}{\mu_R R^2}, \quad \frac{d\varphi_1}{dt} = \frac{L_1}{\mathfrak{S}_1}, \quad \frac{d\varphi_2}{dt} = \frac{L_2}{\mathfrak{S}_2}, \\ \frac{d\ell}{dt} &= -\frac{\partial V}{\partial \theta} - \gamma_{\text{tan}}\left(\frac{\ell}{\mu_R R^2} - \frac{L_1}{\mathfrak{S}_1}a_1 - \frac{L_2}{\mathfrak{S}_2}a_2\right)R \\ &\quad + Rg_{\text{tan}}R_{\text{tan}}(t), \\ \frac{dL_1}{dt} &= -\frac{\partial V}{\partial \varphi_1} + \gamma_{\text{tan}}\left(\frac{\ell}{\mu_R R^2} - \frac{L_1}{\mathfrak{S}_1}a_1 - \frac{L_2}{\mathfrak{S}_2}a_2\right)a_1 \\ &\quad - a_1g_{\text{tan}}R_{\text{tan}}(t), \\ \frac{dL_2}{dt} &= -\frac{\partial V}{\partial \varphi_2} + \gamma_{\text{tan}}\left(\frac{\ell}{\mu_R R^2} - \frac{L_1}{\mathfrak{S}_1}a_1 - \frac{L_2}{\mathfrak{S}_2}a_2\right)a_2 \\ &\quad - a_2g_{\text{tan}}R_{\text{tan}}(t). \end{aligned} \quad (9)$$

The collective coordinates q_i represent z , δ , and α , the symbol p_i denotes momentum conjugated to q_i , and V is the multidimensional potential energy. The symbol ϑ indicates the relative orientation of nuclei. φ_1 and φ_2 stand for the rotation angles of the nuclei in the reaction plane, $a_{1,2} = \frac{R}{2} \pm \frac{R_1 - R_2}{2}$ is the distance from the center of the fragment to the middle point between the nuclear surfaces, and $R_{1,2}$ are the nuclear radii. The symbol R is the distance between the nuclear centers. The total angular momentum $L = \ell + L_1 + L_2$ is preserved. The symbol μ_R is reduced mass, and γ_{tan} is the tangential friction force of the colliding nuclei. Here, it is called sliding friction. The phenomenological nuclear friction forces for separated nuclei are expressed in terms of γ_{tan} and γ_R for sliding friction and radial friction using the Woods-Saxon radial form factor described in Refs. [11]. Sliding and radial friction are described as $\gamma_{\text{tan}} = \gamma_t^0 F(\xi)$ and $\gamma_R = \gamma_R^0 F(\xi)$, where the radial form factor $F(\xi) = [1 + \exp(\frac{\xi - \rho_F}{a_F})]^{-1}$. The model parameters γ_t^0 and γ_R^0 are employed 0.1×10^{-22} MeV s fm⁻² and 100×10^{-22} MeV s fm⁻², respectively. $\rho_F \approx 2$ fm and $a_F \approx 0.6$ fm are also model parameters, determined in Ref. [11], and ξ is the distance between the nuclear surfaces, $\xi = R - R_{\text{contact}}$, where $R_{\text{contact}} = R_1 + R_2$ [11]. The phenomenological friction for the radial direction is switched to one-body friction in the mononucleus stage. γ_R is used to consider the kinetic dissipation according to the surface friction model [28]. The radial friction is calculated as $\gamma_{zz} = \gamma_{zz}^{\text{one}} + \theta(\xi)\gamma_R$. For the mononuclear system, the wall-and-window one-body dissipation γ_{zz}^{one} is adopted for the friction tensor [29–36]. $\theta(\xi)$ is a smoothing function switching the phenomenological friction to that of a mononuclear system as $\theta(\xi) = [1 + \exp(-\frac{\xi}{0.3})]^{-1}$ [11]. m_{ij} and γ_{ij} stand for the shape-dependent collective inertia and friction tensors, respectively. We adopted the hydrodynamical inertia tensor m_{ij}

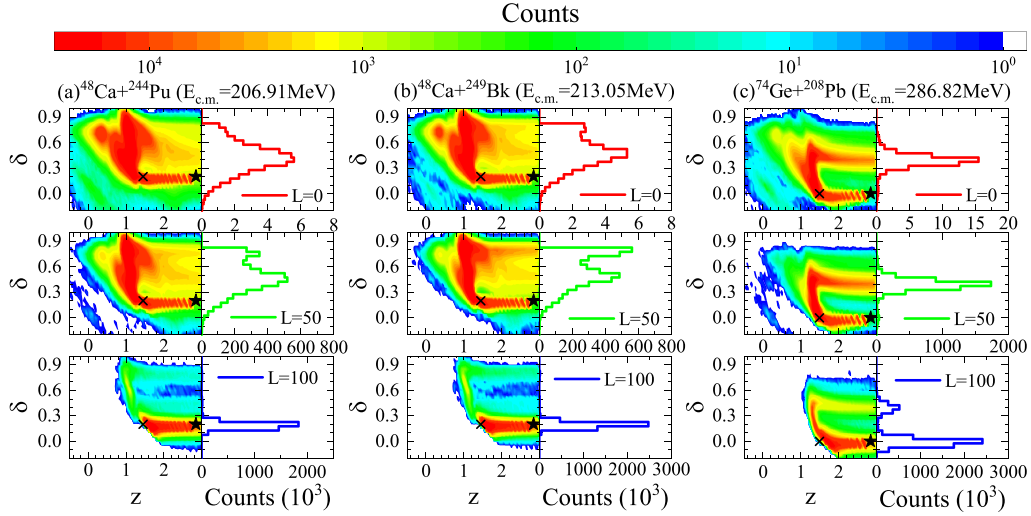


FIG. 2. The distribution of all trajectories and the δ distribution of the deformation of fragments at scission point for the induced orbital angular momenta $L = 0\hbar, 50\hbar, 100\hbar$. The contact point and the starting point of the trajectories are marked by \times and star, respectively.

in the Werner-Wheeler approximation for the velocity field [37]. The one-body friction tensors γ_{ij} are evaluated within the wall-and-window formula [31,38]. The normalized random force $R_i(t)$ is assumed to be white noise: $\langle R_i(t) \rangle = 0$ and $\langle R_i(t_1)R_j(t_2) \rangle = 2\delta_{ij}\delta(t_1 - t_2)$. According to the Einstein relation, the strength of the random force g_{ij} is given as $\gamma_{ij}T = \sum_k g_{ij}g_{jk}$. We start trajectory calculations from a sufficiently long distance between both nuclei [17]. Thus, we use the master equation that takes into account the nucleon transfer for slightly separated nuclei [11,11]. When the separated nuclei achieve the mononucleus state, the neck window of the contact nuclei is sufficiently opened; therefore, the nucleon transfer that occurs in the separated nuclei is almost neglected. Hence, the evolution of the mass asymmetry parameter α switches from the master equation to the Langevin equation in accordance with the procedure described in Ref. [17].

III. RESULTS

A. QF trajectories depending on the initial orbital angular momentum

To review the induced angular momentum dependence of the QF process, the sample trajectories projected on the z - δ plane of the potential energy surface for several orbital angular momenta in the reaction $^{26}\text{Mg} + ^{230}\text{Th}$ ($\alpha = 0.78$) at $E_{\text{c.m.}} = 125.00$ MeV are shown in Fig. 1. The trajectory starts from $\{z, \delta\} = \{2.85, 0.20\}$. In the case of $L = 10\hbar$, it can be seen that the trajectory invades the fusion area. The details of the fusion area are explained in Ref. [17]. The fusion area is defined as $\{|\alpha| < 0.3, \delta < -0.5z + 0.5\}$ in the present calculation. The trajectory for $L = 10\hbar$ does not go towards the direction of fission ($+z$), because it is trapped in the ground state pocket even after ending the calculation. For the $L = 20\hbar$ case, however, the trajectory, after passing through the contact point marked by \times , does not enter the fusion area, and finally the trajectory moves towards the direction of fission ($+z$). This behavior of the trajectory is categorized as the QF reaction. The trajectory for $L = 30\hbar$ also shows the property of the QF

process. At a higher value of L , the barrier indicated by the grey region begins to grow and it is difficult for the trajectories of yet higher L to approach the contact point because of the increasing centrifugal potential energy. These behaviors of trajectories belong to QEC or DIC. In this paper, we treat the QF process as follows.

B. Trajectory distribution on the deformation space

To discuss the dynamics of the fusion-fission process, we introduce the probability distribution of the system in the deformation space. To this end, we segment the coordinate space with $\Delta z = 0.01$, $\Delta\delta = 0.025$, and $\Delta\alpha = 0.001$. We define the distribution as an ensemble of Langevin trajectories. We follow a trajectory as a function of time, and we increase the event number at each segment when the trajectory passes through that segment. By generating many trajectories, we construct a distribution of events on the deformation space [39].

Figure 2 shows the distribution of all trajectories in the z - δ plane for the reaction of $^{48}\text{Ca} + ^{244}\text{Pu}$, $^{48}\text{Ca} + ^{249}\text{Bk}$, and $^{74}\text{Ge} + ^{208}\text{Pb}$ systems with $E_{\text{c.m.}} = 206.91$ MeV, $E_{\text{c.m.}} = 213.05$ MeV, and $E_{\text{c.m.}} = 286.82$ MeV, respectively. Here, the Langevin calculations are stopped at $t = 10^{-19}$ s. The δ distributions of the deformation of fragments at the scission point are also appended to the figure as histograms for $L = 0\hbar, 50\hbar$, and $100\hbar$. The trajectories start at the point marked with a star, $\{z, \delta\} = \{2.85, 0.20\}$ for the $^{48}\text{Ca} + ^{244}\text{Pu}$ and $^{48}\text{Ca} + ^{249}\text{Bk}$ systems and $\{z, \delta\} = \{2.85, 0.00\}$ for the $^{74}\text{Ge} + ^{208}\text{Pb}$ system. The initial value $\delta = 0$ is set for the spherical nuclear case. The contact point is denoted as \times .

In Figs. 2(a) and 2(b), for the central collision ($L = 0\hbar$) the trajectories near the scission point distribute around $\delta \approx 0.4$, but for $L = 50\hbar$ the distribution has a structure with two peaks. The different quasifission modes appear in this angular momentum region. In the case of the $^{48}\text{Ca} + ^{249}\text{Bk}$ system, the structure of the δ distribution appears even for the low partial wave, and the bifurcation of the trajectory can be seen

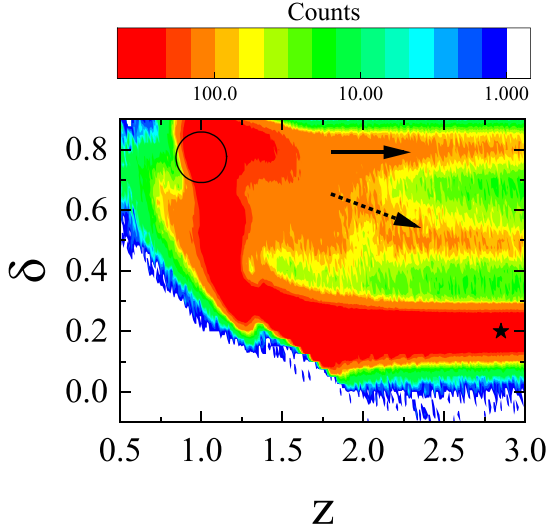


FIG. 3. The trajectory distribution for $^{48}\text{Ca} + ^{249}\text{Bk}$ system with $E_{c.m.} = 213.05$ MeV and $L = 50\hbar$. Starting at star point $\{z, \delta\} = \{2.85, 0.20\}$, passing through the bifurcation point of paths marked with the symbol BP(\circ), the trajectory evolves toward different areas indicated by arrows. The path along the solid arrow is named “path1” and the dashed arrow “path2.”

clearly. As the Coulomb interaction is stronger in this system, the approach to the fusion area is inhibited. The mode that appeared in the δ distribution has a different timescale, as discussed later. In contrast, in the $^{74}\text{Ge} + ^{208}\text{Pb}$ system, no bifurcation in the quasifission path can be seen because of the entrance memory of the strong shell effect of the target ^{208}Pb . From the starting point (\star), the fragment deformation increases only up to $\delta \approx 0.6$ owing to the stiffness of ^{208}Pb . Therefore, the trajectory follows a similar area leading to the same fragment deformation around $\delta \approx 0.4$. We select a typical example of the QF path bifurcation from Fig. 2(b).

Figure 3 shows an enlarged map of the trajectory distribution for the $^{48}\text{Ca} + ^{249}\text{Bk}$ system ($L = 50\hbar$). From the starting point indicated by the star, the trajectory moves to the area of large δ up to 0.8 where the fragments are stretched in preparation of fission. Then, the fission path bifurcates at the point $\{z, \delta\} = \{1.3, 0.8\}$, and each path evolves along the arrows. We call the trajectory sustaining $\delta = 0.8$ “path1,” indicated by the solid arrow, and the other trajectory along the dashed arrow “path2.” The interesting point is the timescales of these two paths, which lead to the different fragment mass distributions, as shown in the next section.

C. Two quasifission modes in massive nucleon transfer

Figure 4 shows the fragment mass distributions for path1 and path2. The components of path1 and path2 correspond to the deformation ranges of $0.6 < \delta < 0.8$ and $0.4 < \delta < 0.6$ at the scission point, respectively. The main peak of the fragment distributions is located far outside the symmetric region of $A_{CN}/2 \pm 20$ u. Therefore, the normalized measure of the degree of mass drift toward the symmetry defined by Shen *et al.* [1] $\Delta A/\Delta A_{\max}$ is less than ≈ 0.3 , where $\Delta A/\Delta A_{\max} = \frac{1}{2}(A_t - A_p)$ and $\Delta A = A_f - A_p$. A_f , A_t , and A_p are the fragment, target,

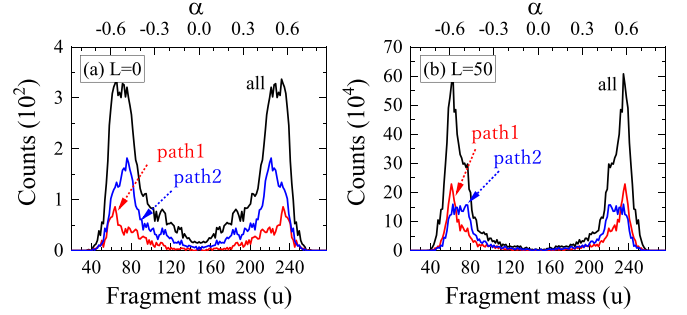


FIG. 4. The fission fragment mass distribution for the $^{48}\text{Ca} + ^{249}\text{Bk}$ system with $E_{c.m.} = 213.05$ MeV and $L = 50\hbar$. The distributions in path1 and path2 are plotted separately by the red and the blue lines, respectively. Panel (a) is for $L = 0\hbar$ and (b) for $L = 50\hbar$.

and projectile mass, respectively. Since both QF modes have a large elongation, no sign of the spherical fission fragment such as Pb can be seen. However, the mass distribution shows a subtle difference. The peak of mass distribution for path2 shifts to the mass symmetric region, in comparison with that of path1. It is inferred that the mass drift is larger than that in path1, as can be seen from the trajectory distribution plotted in the z - α plane shown in Fig. 5, where the trajectory distribution of path2 extends to the lower value of α . We further investigate the dynamics around the bifurcation point (BP) of two modes near $\delta = 0.8$. The feature of the trajectory bifurcation and the shape of fissioning nuclei are drawn in Fig. 6. The illustrations of fragment shape for path1 and path2 are distinguished by red and blue colors, respectively. The striking fact is in the role of neck radius for each path. The small neck radius of path1 inhibits the mass drift at this point. On the one hand, the nuclear shape of path2 has a large neck radius and the mass drift can be sustained after passing BP. As a result, the fragment mass distribution for path2 shifts further to the mass symmetric region. These differences originate from the fluctuation in the timescale of the reaction. As shown in Fig. 7(a), path2 belongs to the time-consuming trajectory to reach BP in comparison with path1. The evolution degree of deformation

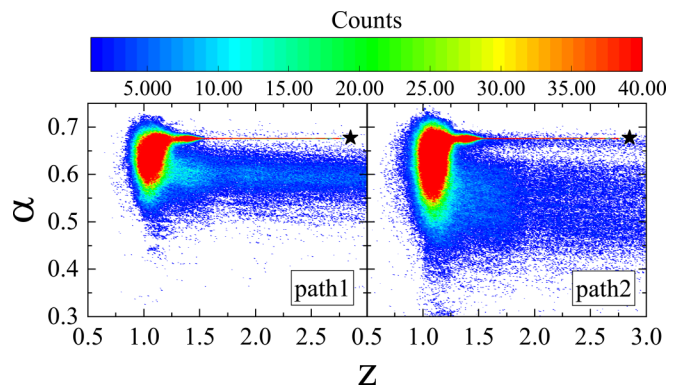


FIG. 5. The trajectory distribution of path1 and path2 drawn in the z - α plane for the $^{48}\text{Ca} + ^{249}\text{Bk}$ system with $E_{c.m.} = 213.05$ MeV and $L = 50\hbar$. The starting points of the trajectories are denoted by star symbols.

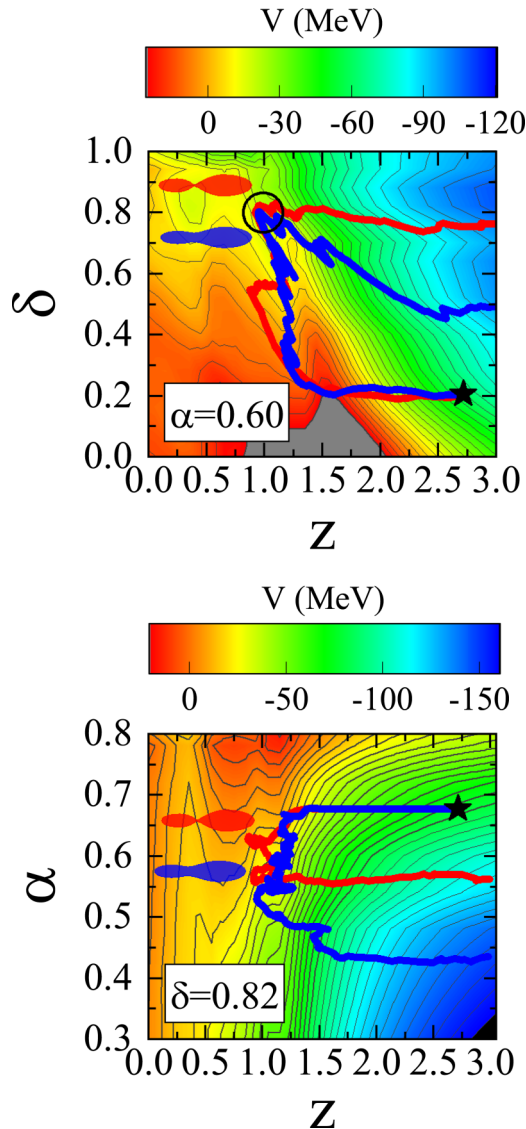


FIG. 6. The feature of the trajectory bifurcation and the shape of fissioning nuclei for $^{48}\text{Ca} + ^{249}\text{Bk}$ system with $E_{\text{c.m.}} = 213.05$ MeV and $L = 50\hbar$. The bifurcation point and the starting point of the trajectories are indicated by \circ and star, respectively.

in each path shows the sample results. The times that the sample trajectories of path1 and path2 reach BP are ≈ 5.6 zs and ≈ 10.8 zs. The distribution of the time duration for each path to reach the area of BP is shown in Fig. 7(c). Owing to the random fluctuation of the trajectory combined in the potential energy surface (PES), the time duration to obtain BP also fluctuates. It takes ≈ 9 zs on average for path2. In addition, the important point is in the behavior of the time evolution of the neck parameter ϵ in Fig. 7(b). The trajectory of path1 reaches the scission point before the neck parameter decreases sufficiently toward the recommended value for fission, $\epsilon \approx 0.35$ [26] in Eq. (8). It is mentioned that the value can be extracted from the analyses of the mass and energy distributions of the fission fragments [9]. In Fig. 7, we employ $t_0 = 9.0 \times 10^{-21}$ s and $\Delta_\epsilon = 1.0 \times 10^{-21}$ s in Eq. (8).

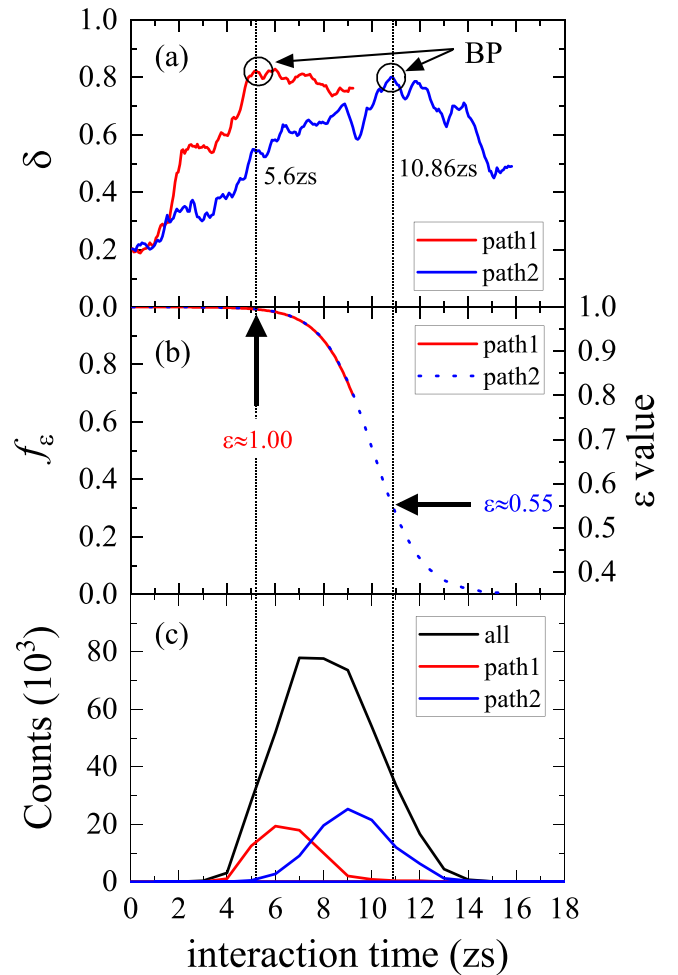


FIG. 7. The temporal evolution of the trajectory (a) and the neck parameter ϵ (b) for the two different paths in the $^{48}\text{Ca} + ^{249}\text{Bk}$ system with $E_{\text{c.m.}} = 213.05$ MeV and $L = 50\hbar$. The distributions of the time duration reaching BP for different paths are plotted in (c). In all panels, vertical dotted lines indicate the time of reaching BP labeled in panel (a).

It is clear that, as shown in Fig. 7(b), the neck parameter ϵ for each path differs at BP, i.e., $\epsilon \approx 1.0$ for path1 and $\epsilon \approx 0.55$ for path2. The neck radius near the scission point is strongly related to the timescale of the trajectory mentioned above. It is inferred that sufficient relaxation of the neck condition further accelerates the mass drift. For the trajectory taking a long time to reach BP, i.e., path2, the value of ϵ is decreased to 0.55. In contrast, if the trajectory reaches BP in a short time, i.e., path1, neck relaxation is incomplete and mass drift stops at that point.

This situation can be seen clearly in Fig. 8, where the contour map of the neck cross section is drawn in the z - δ plane overwriting the trajectory of each path. We can see that the neck cross section vanished at BP for path1 but still exists for path2. Therefore, in path2, the mass drift continues after passing BP owing to the decrease in ϵ , as shown in Fig. 7.

Here, we investigate the TKE of fission fragments to distinguish two modes. The scission configuration is defined as the shape with the neck radius equal to zero [40]. The TKE is

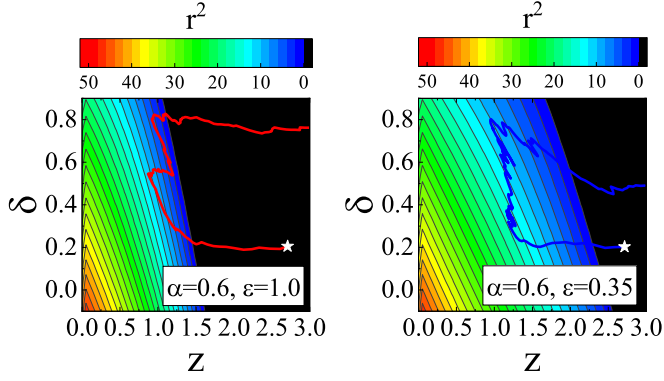


FIG. 8. The contour map of the square of neck radius r^2 in the same $^{48}\text{Ca} + ^{249}\text{Bk}$ system as in Fig. 7. The trajectories of path1 (left) and path2 (right) are overwritten. The trajectories start at the points marked by stars.

expressed as

$$\text{TKE} = V_{\text{coul}} + E_{\text{pre}}, \quad (10)$$

$$V_{\text{coul}} = e^2 \frac{Z_1 Z_2}{d_{\text{sci}}}, \quad (11)$$

$$E_{\text{pre}} = \frac{1}{2} (m^{-1})_{ij} p_i p_j, \quad (12)$$

where E_{pre} and V_{coul} denote the prescission kinetic energy and the prescission Coulomb energy, respectively. $e^2 = 1.44 \text{ MeV fm}$, Z_1, Z_2 are the charges of each fragment, and d_{sci} is the distance between the centers of mass of light and heavy parts of the nucleus at the scission point. The average of E_{pre} over all fission events is equal to 7.03 MeV. Thus, the main contribution to the TKE comes from the Coulomb repulsion of fission fragments.

Figure 9 shows the calculation results of TKE shown by each path at $L = 50\hbar$. The TKE of each path differs owing to different d_{sci} values. The average TKE values of each path are $\langle \text{TKE}_{\text{path1}} \rangle = 119 \text{ MeV}$ and $\langle \text{TKE}_{\text{path2}} \rangle = 145 \text{ MeV}$. The lower TKE corresponds to a more elongated scission configuration (path1). The TKE values shown by path1 and path2 are different, and two modes clearly exist in QF.

IV. CONCLUSIONS

The dynamical characteristics of the QF processes were investigated in terms of the Langevin equation model. We

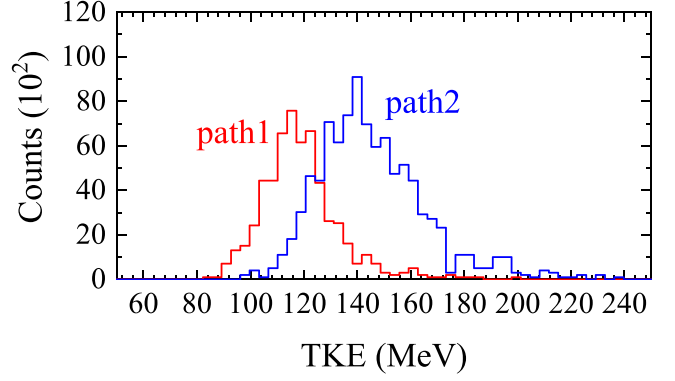


FIG. 9. The TKE distribution in the same $^{48}\text{Ca} + ^{249}\text{Bk}$ system as in Fig. 7. The red and blue lines indicate path1 and path2, respectively.

paid attention to the QF processes outside the fragment mass of $A_{\text{CN}}/2 \pm 20 \text{ u}$ and the inside DIC processes with several nucleon transfers. The $^{48}\text{Ca} + ^{249}\text{Bk}$ system was taken as an example. Detailed dynamical analysis of the QF trajectory in the Langevin calculation was performed. It was found that there exist two QF modes with different fragment mass and deformations. Results of the trajectory analysis revealed that the characteristics of each mode originates from the different timescales of the reaction, which arise from the different neck relaxation modes controlling the mass drift toward mass symmetry. This means that it is possible to discuss the time-dependent functional form of the neck parameter ϵ during the QF process in the framework of the Langevin equation model. Note that the relaxation of the neck parameter is sensitive to the structure of the QF mass fragment distribution. The scission configurations of the two modes are both very elongated. However, one of the two modes corresponds to a more elongated scission configuration. The characteristics of two QF modes may lead to useful knowledge in the experimental QF analyses. We hope that the difference of TKE values of the QF component in the medium angular momentum (impact parameter) region can be confirmed experimentally using collision systems forming $Z \geq 114$ with hot fusion.

ACKNOWLEDGMENTS

The Langevin calculation was performed using the cluster computer system (Kindai-VOSTOK) under the support of JSPS KAKENHI Grant No. 20K04003 and Research funds for External Fund Introduction 2021 provided by Kindai University.

- [1] W. Q. Shen *et al.*, *Phys. Rev. C* **36**, 115 (1987).
- [2] B. B. Back *et al.*, *Phys. Rev. C* **53**, 1734 (1996).
- [3] M. G. Itkis *et al.*, *Nucl. Phys. A* **944**, 204 (2015).
- [4] E. M. Kozulin *et al.*, *Phys. Rev. C* **90**, 054608 (2014).
- [5] E. M. Kozulin *et al.*, *Phys. Rev. C* **94**, 054613 (2016).
- [6] E. M. Kozulin *et al.*, *Phys. Rev. C* **99**, 014616 (2019).
- [7] A. Diaz-Torres, G. G. Adamian, N. V. Antonenko, and W. Scheid, *Phys. Rev. C* **64**, 024604 (2001).

- [8] A. V. Karpov and V. V. Saiko, *Phys. Rev. C* **96**, 024618 (2017).
- [9] V. Zagrebaev *et al.*, *Phys. Part. Nuclei* **38**, 469 (2007).
- [10] V. Zagrebaev and W. Greiner, *J. Phys. G: Nucl. Part. Phys.* **34**, 2265 (2007).
- [11] V. Zagrebaev and W. Greiner, *J. Phys. G: Nucl. Part. Phys.* **31**, 825 (2005).
- [12] G. Bertsch, *Z. Phys. A* **289**, 103 (1978).
- [13] W. Cassing and W. Nörenberg, *Nucl. Phys. A* **401**, 467 (1983).

- [14] A. Diaz-Torres, *Phys. Rev. C* **69**, 021603(R) (2004).
- [15] J. Maruhn and W. Greiner, *Z. Phys.* **251**, 431 (1972).
- [16] K. Sato *et al.*, *Z. Phys. A* **288**, 383 (1978).
- [17] Y. Aritomo and M. Ohta, *Nucl. Phys. A* **744**, 3 (2004).
- [18] H. J. Krappe, J. R. Nix, and A. J. Sierk, *Phys. Rev. C* **20**, 992 (1979).
- [19] V. Strutinsky, *Nucl. Phys. A* **122**, 1 (1968).
- [20] M. Brack *et al.*, *Rev. Mod. Phys.* **44**, 320 (1972).
- [21] S. Suekane, A. Iwamoto, S. Yamaji, and K. Harada, JAERI Report No. 5918, 1993 (unpublished).
- [22] A. Iwamoto *et al.*, *Prog. Theor. Phys.* **55**, 115 (1976).
- [23] S. G. Nilsson *et al.*, *Nucl. Phys. A* **131**, 1 (1969).
- [24] Y. Aritomo, S. Chiba, and F. Ivanyuk, *Phys. Rev. C* **90**, 054609 (2014).
- [25] A. V. Ignatyuk, G. N. Smirenkin, and A. S. Tishin, *Yad. Fiz.* **21**, 485 (1975).
- [26] S. Yamaji, H. Hofmann, and R. Samhammer, *Nucl. Phys. A* **475**, 487 (1987).
- [27] Y. Aritomo, *Phys. Rev. C* **80**, 064604 (2009).
- [28] P. Fröbrich and I. I. Gontchar, *Phys. Rep.* **292**, 131 (1998).
- [29] J. Blocki *et al.*, *Ann. Phys. (NY)* **113**, 330 (1978).
- [30] J. Rayford Nix and A. J. Sierk, *Nucl. Phys. A* **428**, 161 (1984).
- [31] J. Randrup and W. Swiatecki, *Nucl. Phys. A* **429**, 105 (1984).
- [32] H. Feldmeier, *Rep. Prog. Phys.* **50**, 915 (1987).
- [33] N. Cârjan, A. J. Sierk, and J. R. Nix, *Nucl. Phys. A* **452**, 381 (1986).
- [34] N. Cârjan, T. Wada, and Y. Abe, in *Towards a Unified Picture of Nuclear Dynamics*, 6–8 June 1991, Nikko, Japan, AIP Conf. Proc. No. 250 (AIP, New York, 1992), p. 230.
- [35] T. Wada, Y. Abe, and N. Carjan, *Phys. Rev. Lett.* **70**, 3538 (1993).
- [36] T. Asano *et al.*, *J. Nucl. Radiochem. Sci.* **7**, 7 (2006).
- [37] K. T. R. Davies, A. J. Sierk, and J. R. Nix, *Phys. Rev. C* **13**, 2385 (1976).
- [38] A. J. Sierk and J. R. Nix, *Phys. Rev. C* **21**, 982 (1980).
- [39] Y. Aritomo, K. Hagino, K. Nishio, and S. Chiba, *Phys. Rev. C* **85**, 044614 (2012).
- [40] Y. Aritomo and S. Chiba, *Phys. Rev. C* **88**, 044614 (2013).